Advances in Science and Technology Research Journal

Advances in Science and Technology Research Journal, 2026, 20(3), 336–349
https://doi.org/10.12913/22998624/213614
ISSN 2299-8624, License CC-BY 4.0

Received: 2025.09.17
Accepted: 2025.11.25
Published: 2026.02.01

Thermoplastic processing of grade 2 titanium: Finite element method simulations and experimental validation with the Anand model

Jakub Bańczerowski[1]

[1] Faculty of Mechanical and Industrial Engineering, Warsaw University of Technology, ul. Narbutta 85, 02-524 Warsaw, Poland
E-mail: jakub.banczerowski@pw.edu.pl

ABSTRACT

This work examined thermoplastic processing (TMP) of commercially pure Grade 2 titanium using finite element simulations with the Anand viscoplastic constitutive model and a broad experimental validation matrix (400–800 °C; 0.01–10 s^{-1}, including an intermediate 5 s^{-1} case). The goal was to assess whether this model, originally developed for solder alloys, can capture the deformation behaviour of titanium at elevated temperatures, relevant to biomedical applications. Uniaxial compression tests were performed at 400–800 °C and strain rates of 0.01–10 s^{-1}, and the resulting stress–strain curves were compared with the FEM simulations in Ansys Workbench. Parameter calibration was based on experimental data, with focus on 500–600 °C and 0.1–1 s^{-1} - conditions previously shown to promote grain refinement and mechanical strengthening. The Anand model reproduced stress evolution well in the initial deformation phase, particularly at lower strain rates. Stress distributions in the FEM simulations captured the expected axial stress gradients (centre < side < edge), while stresses were typically 30–40 MPa higher than measured. The model also reproduced the elastic–plastic transition, with smoother behaviour observed at higher temperatures. However, the model does not account for dynamic recrystallisation (DRX) or related softening mechanisms, which leads to overestimation of stresses in the later stages of deformation. Experimental samples also displayed anisotropic deformation, likely due to initial material texture, which was not represented in the model. Despite these limitations, the Anand formulation demonstrates potential for predicting TMP of pure titanium, reducing reliance on trial-and-error testing and supporting process optimisation for biomedical applications.

Keywords: thermoplastic deformation, FEM, Anand model.

INTRODUCTION

Titanium, due to its biocompatibility, is widely used in biomedical engineering, for example as a material for implants [1, 2]. For the prostheses subjected to high loads (e.g., hip joint endoprostheses), pure titanium is unsuitable because of its relatively low strength (~345 MPa). Instead, Ti6Al4V alloy (~950 MPa) is commonly used [3]. However, long-term exposure to vanadium and aluminium ions is toxic to the human body [4–6]. Using commercially pure Grade 2 titanium eliminates these elements but leaves an insufficient strength margin. Thermomechanical processing (TMP) refines the grain structure and increases flow stress, narrowing the gap to Ti-6Al-4V while preserving the benign chemistry of pure Ti [7–9].

According to Hall-Petch relation grain refinement lead to material strength [7, 8]. Due to titanium HCP crystal structure, cold-forming of this material is difficult and therefore the thermomechanical processing (TMP) is proposed [9]. At intermediate temperatures (400–600 °C); however, the combined effects of strain hardening and dynamic recovery produce highly nonlinear stress–strain behaviour. This complexity complicates process optimisation, with current approaches relying heavily on trial-and-error experimentation, consuming significant time and resources.

The aim of this study was to develop and validate a numerical model reproducing the thermoplastic processing of commercially pure Grade 2 titanium under elevated temperature and varying strain rates. Phenomenological constitutive models are particularly useful for such purposes. In earlier work, several models were considered, including Arrhenius, Johnson-Cook, Khan-Huang-Liang and Anand models [10]. Arrhenius-type (Zener–Hollomon) equations correlate peak/steady stresses with the parameter, but remain purely phenomenological and are typically calibrated to quasi-steady flow; they require many temperature-specific fits, provide no internal state to track deformation resistance, and extrapolate poorly across strain-rate/temperature histories [11]. The Johnson–Cook (JC) model expresses flow stress as separable multiplicative functions of strain, strain rate, and temperature; while robust for moderate temperatures and impact/ballistic rates, JC does not account for time-dependent recovery and offers weak coupling between rate- and temperature-sensitive softening, which leads to overprediction under warm forming (400–600 °C) at low-to-intermediate rates and poor transient response without ad-hoc corrections [11]. The Khan–Huang–Liang family improves rate–temperature coupling (and can represent twinning), but involves numerous constants and is not natively supported in many commercial FEM environments [11, 12]. In contrast, the Anand formulation introduces a single internal state variable s (deformation resistance) with a thermally activated evolution law that naturally captures strain-rate sensitivity and dynamic recovery under non-proportional loading; it is also directly available in Ansys, facilitating process-level simulations [13–15]. Its main limitation—no explicit dynamic-recrystallisation softening term—is acknowledged here; nevertheless, within the targeted 500–600 °C and 0.1–1 s^{-1} window for grain refinement, Anand reproduces the initial and near-saturation flow with acceptable accuracy and numerical robustness, which motivated its selection in this study [10, 11, 15].

The objective was to assess whether the Anand model—originally developed for other materials—can effectively describe the viscoplastic deformation of titanium. A central aspect of the study is the comparison of finite element simulations with experimental data, identifying the conditions under which the model provides accurate predictions and where its limitations become apparent.

This study is a follow up of the previous investigation of commercially pure titanium TMP at intermediate temperatures to achieve the yield strengths required for orthopaedic implants [16], exploring key differences between real process and FEM simulation. Finally, a quantitative methodology that connects calibrated model parameters with underlying microstructural evolution mechanisms was proposed. This approach not only improves the accuracy of flow stress predictions under both tested and extrapolated processing conditions but also provides deeper insight into the physical processes governing high-temperature plasticity in titanium.

In biomedical forming processes of titanium, typical flow stresses at intermediate temperatures are in the range of 150–400 MPa [9, 17, 18]. Therefore, a deviation of 30–40 MPa represents an error of roughly 10%, which is generally considered acceptable for phenomenological constitutive models used in process design [19, 20]. Such discrepancies are unlikely to affect the feasibility of the forming process, but they do limit the precision of predictive modelling for microstructural evolution.

METHODS

Thermomechanical processing (TMP)

This study focused on compressive thermomechanical processing relevant to upsetting/forging steps used prior to final shaping of biomedical components. In the 400–600 °C, 0.01–10 s^{-1} window, tension on Grade 2 Ti is prone to early necking, compromising constitutive calibration with geometry-dependent artefacts. Torsion requires dedicated hardware and yields non-uniform shear/temperature fields, hindering comparison with the Gleeble compression setup. Uniaxial compression permits large stable strains, aligns with the targeted route, and provides the most reliable flow-stress data for FEM; hence it is the primary, representative mode for model identification.

According to EBSD analysis, mean grain size of the sample was 6.06 μm (with median equal 5.22 μm). The hardness of the undeformed sample equals 200.4 on the HV 0.2 scale [21]. Detailed microstructural evidence of grain refinement in the targeted TMP window (SEM/EBSD maps,

grain-size distributions, and hardness) has been reported previously for the same Grade 2 Ti stock and processing conditions; key results are summarised here and the full dataset is provided in [21].

The TMP applied to this material involved uniaxial compression of titanium samples with dimensions of ⌀10 × 12 mm at elevated temperatures (ranging from 400 °C to 800 °C) and strain rates between 0.01 s^{-1} and 10 s^{-1}. The samples were machined from hot-rolled bars, with the longitudinal axis aligned parallel to the rolling direction to maintain microstructural consistency. The full experimental plan is presented in Table 1. Each test case was performed at least three times in order to maintain statistical significance. To reduce friction-induced non-uniform deformation (barreling), tantalum and graphite foils together with a graphite-based lubricant were placed between the specimen ends and tool surfaces. Temperature was monitored and controlled using two type-K thermocouples on the specimen side. The specimens were resistively heated via anvils (with maximum heating rate 10,000 °C/s) and tests were conducted in vacuum to minimise the effect of oxide scale. The compression was performed using a Gleeble 3800 TMP simulator – the setup of the experiment is shown in Figure 1.

The samples deformed in an unexpected manner. It was anticipated that the compressed specimens would be axially symmetric with a barrel-like shape. In this case, however, the samples showed a tendency to deform more strongly in one direction, suggesting a certain degree of material anisotropy, most likely related to non-uniform rolling during the production of the rod (Figure 2).

The best results in terms of grain refinement were obtained for the samples deformed at 500–600 °C and strain rates of 0.1–1 s^{-1}; therefore, these conditions were selected for further considerations regarding the numerical model [21].

Stress–Strain curves

The results were recorded in the form of stress–strain curves, with stress and strain values calculated using Equations 1 and 2.

$$\varepsilon = \ln\frac{L_0 + \Delta L}{L_0} \tag{1}$$

$$\sigma = \frac{F}{\left[\frac{\pi d_0^2}{4}\cdot\frac{L_0}{L_0 + \Delta L}\right]} \tag{2}$$

Table 1. Complete plan of the compression experiment

Sample designation	Temperature	Strain rate [s^{-1}]	No. of performed tests
p1	400 °C (673 K)	0.01	4
p2		0.1	3
p3		1	3
p4		10	4
p17	500 °C (773 K)	0.01	2
p18		0.1	2
p19		1	2
p20		10	3
p13	600 °C (873 K)	0.01	2
p14		0.1	2
p15		1	4
p16		10	4
p5	700 °C (973 K)	0.01	4
p6		0.1	3
p7		1	3
p8		10	3
p9	800 °C (1073 K)	0.01	3
p10		0.1	3
p11		1	3
p12		10	3

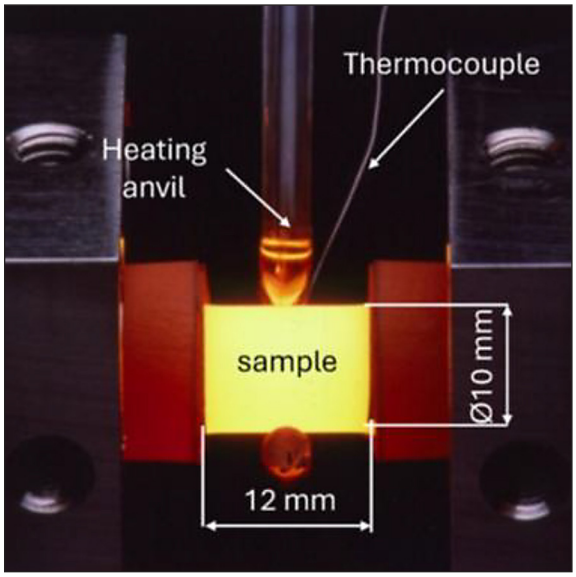

Figure 1. Gleeble 3800 compression setup

where: L_0 is the initial length of the sample (12 mm), ΔL is the length change after compression, d_0 is original diameter of the sample (10 mm).

The stress–strain curves recorded during TMP show that stresses decrease with increasing temperature and rise with increasing strain rate. At higher temperatures, the curves exhibit a shape characteristic of viscoplastic materials: after the elastic stage, a plastic stage follows with a progressively flattening curve (Figure 2) [22–24]. In some cases (e.g., at strain rates of 1 s^{-1} and 10 s^{-1}), a drop in stress after reaching the peak can also be observed. This indicates the occurrence of the so-called three-stage work hardening process [11, 24, 25]. In Stage I, work hardening dominates and stress increases sharply. In Stage II, the effects of dynamic recovery (DRV) and dynamic recrystallisation (DRX) appear, slowing down the stress increase. In Stage III, stress decreases as recovery and recrystallisation mechanisms prevail [11, 26].

Slight serration of the stress-strain curves was also observed (especially for the higher strain rates) The curve shape indicates the Portevin–Le Chatelier effect, commonly observed in metals though driven by different mechanisms [27, 28]. For α-titanium, Prasad explained this behaviour as mobile dislocations being pinned by interstitial elements such as C and N, then breaking free and rapidly moving to the next obstacle (Figure 3), producing the characteristic serrations [29].

Standard deviation was calculated, but due its low value and massive number of measurement points (over 9000 in the case of $\dot{\varepsilon}$ = 0.01 s-1) visibility of error bars on stress-strain graphs was limited; therefore, this information is supplemented in Table 2 below, providing mean ± SD at a few anchor strains (ε = 0.20–0.80).

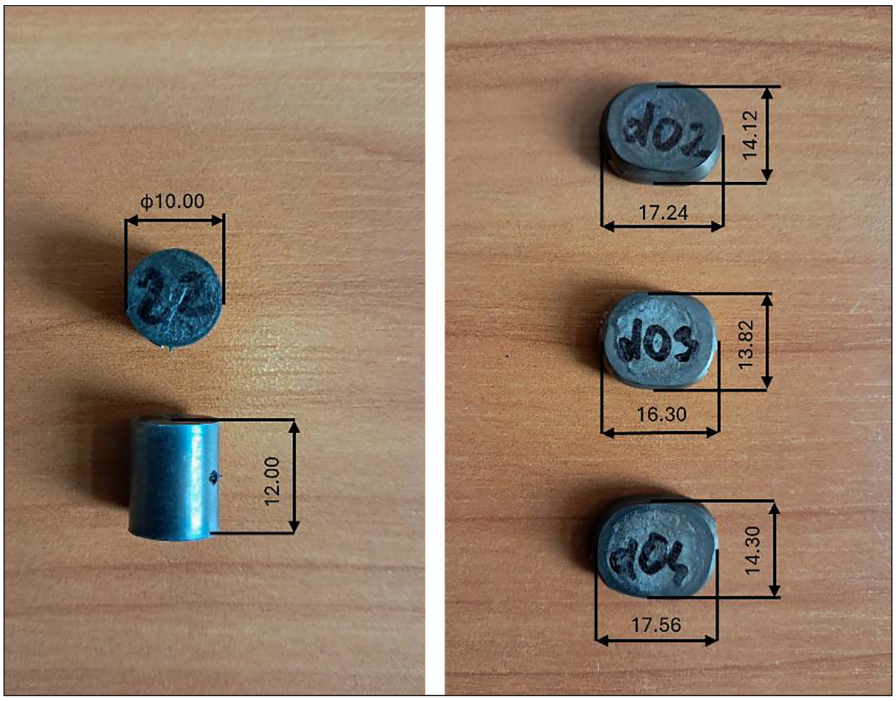

Figure 2. Titanium samples before (left – height 12 mm, diameter 10 mm) and after (right) an experiment. Dimensions are in mm

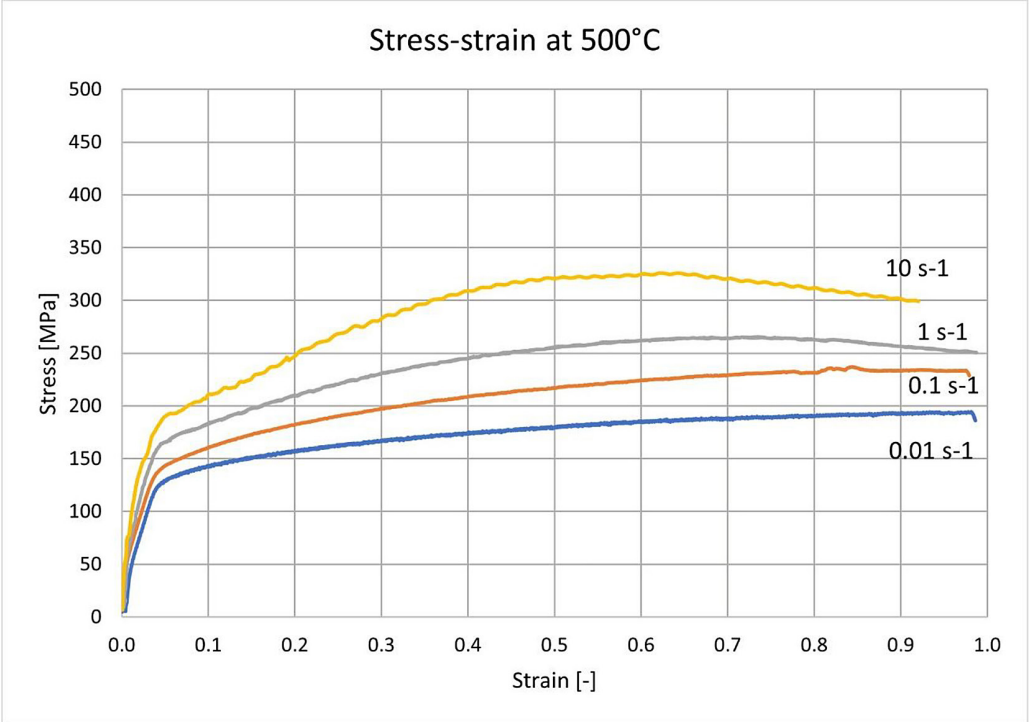

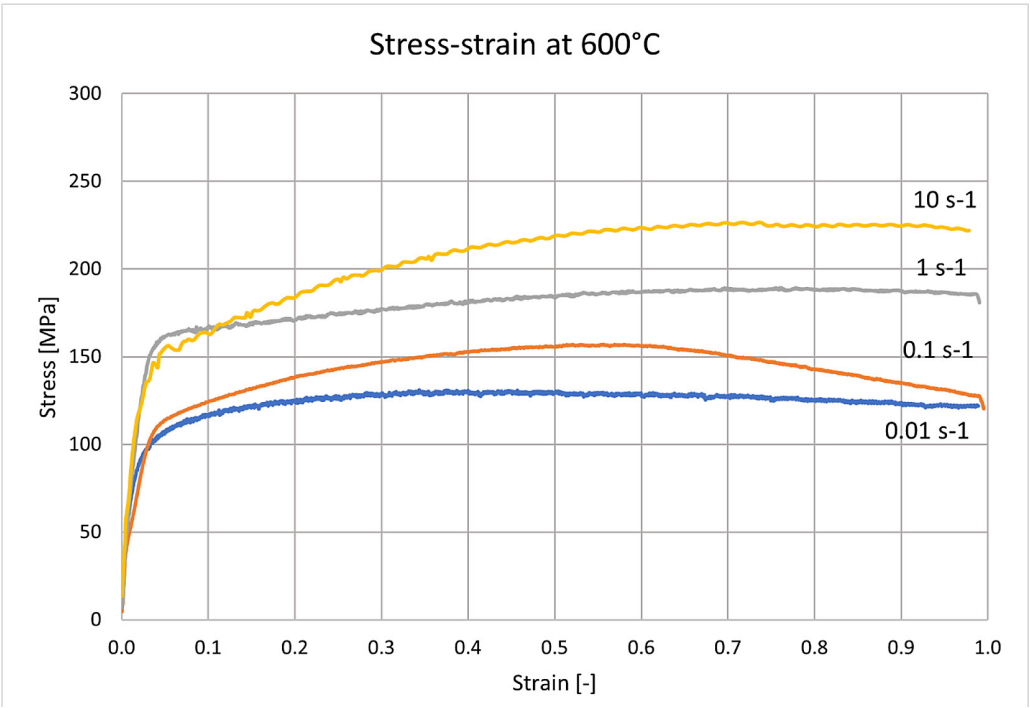

Figure 3. Stress-strain graph for 500 °C and 600 °C

Anand model

The viscoplastic behaviour of the material at elevated temperatures provided the motivation to apply a mathematical model that is rather uncommon for TMP. The Anand model [13, 14] was selected, which is most frequently used to describe solder alloys [30–32]. The Anand model reflects the influence of strain rate and temperature sensitivity, while also accounting for strain hardening and dynamic recovery.

In simplified form, the Anand model can be expressed as follows:

$$\sigma^* = \frac{\hat{s}}{\xi}\left[\frac{\dot{\varepsilon_p}}{A}\exp\frac{Q}{RT}\right]^n \sinh^{-1}\left\{\left[\frac{\dot{\varepsilon_p}}{A}\exp\frac{Q}{RT}\right]^m\right\} \quad (3)$$

Table 2. Standard deviation of measured flow stress (MPa) at selected strains for Grade 2 Ti: 500 and 600 °C, strain rates 0.01–10 s^{-1}

Strain [–]	Standard deviation of measured stress [MPa]							
	500 °C				600 °C			
	0.01 s^{-1}	0.1 s^{-1}	1 s^{-1}	10 s^{-1}	0.01 s^{-1}	0.1 s^{-1}	1 s^{-1}	10 s^{-1}
0.2	0.4012	0.3395	2.6549	8.2414	0.4310	0.8605	11.7358	10.2538
0.4	0.0572	2.6132	1.1692	6.0190	0.2584	1.0499	6.3507	6.6941
0.6	0.1936	4.0707	0.1264	4.7215	0.5438	1.2000	2.6681	4.8335
0.8	0.1648	3.3455	4.4856	3.9499	0.4542	0.0524	4.4856	3.9499

The full form of the equation is as follows:

$$\sigma = \sigma^* - \left[\begin{matrix} (\sigma^* - cs_0)^{1-a} + \\ + (a+1)\{(ch_0)(\sigma^*)^{-a}\}\varepsilon_p \end{matrix} \right]^{1/(1-a)} \quad (4)$$

The constant h_0 represents the hardening/softening coefficient, s_0 is the initial value of s, and a is the strain rate sensitivity for hardening/softening processes.

A c parameter is a function of strain rate and temperature, defined as

$$c = \frac{1}{\xi}\sinh^{-1}\left\{\left[\frac{\dot{\varepsilon_p}}{A}\exp\left(\frac{Q}{RT}\right)\right]^m\right\} \quad (5)$$

To correctly apply the Anand model in numerical analysis, the following constants must be determined: $A, Q, \xi, m\,\hat{s}, n, h_0, a, s_0$. In order to do so, first saturation stress (s) value had to be extracted from the stress-strain curves. Then, constants $A, Q, \xi, m\,\hat{s}, n$ were determined using Equation 3 and the least squares method. The ξ fraction was treated here as a single parameter. Those two were derived from the previous step, with ξ adjusted to keep c (Equation 5) around unity. Then, $\hat{s}$ was determined from $\hat{s}/\xi$. Finally, constants ch_0, cs_0, a (Eq. 2.32) were calculated using nonlinear least squares from constant strain rate data. With c known, h_0 and s_0 were then obtained. Model parameters at the target temperatures (500 and 600 °C) are listed in Table 3; nonlinear-fit statistics are reported in Table 4. Across all, conditions the fits are strong (R^2 = 0.97–0.995) with low absolute errors (RMSE = 4–13 MPa, ≈1–6% of flow stress), with the largest deviations at 500 °C–10 s^{-1} where dynamic softening becomes most pronounced and is not explicitly represented by the Anand model.

Numerical analysis

The aim of the numerical analyses was to verify the correct implementation of the Anand model by comparing the simulation results with experimental data. Additionally, for validation purposes, a simulation was performed at a strain rate of 5 s^{-1}, with the expectation that the resulting stresses would fall between those obtained for 1 s^{-1} and 10 s^{-1}. Faithful reproduction of the actual compression test conditions was critical.

Table 3. Calibrated Anand model parameters for Grade 2 Ti at 500 °C and 600 °C

Temp.	Q [J/mol]	S_0[MPa]	A	ξ	m	n	$\hat{s}$	n	a	$\hat{s}/\xi$	c
500 °C	301000	8.55	1.25E+05	25.00	0.747	10000	26.13	0.064	3.482	1.045	0.862
600 °C	300000	4.56	1.49E+05	29.00	0.973	7609	44.69	0.060	1.610	1.541	0.837

Table 4. Anand model statistical fit metrics for Grade 2 Ti at 500 °C and 600 °C

Temp.	500 °C				600 °C			
$\dot{\varepsilon}$ [1/s]	0.01	0.1	1	10	0.01	0.1	1	10
SSE	2347	1002	2700	8833	1582	3211	1819	1157
R-square	0.985	0.9944	0.988	0.9783	0.9884	0.9698	0.9815	0.9924
Adjusted R-square	0.9846	0.9941	0.9872	0.977	0.988	0.9681	0.9808	0.9919
RMSE	4.97	4.476	7.579	13.29	3.941	7.641	6.157	4.545

The TMP simulations were carried out in Ansys Workbench 2020R. For each temperature, a separate project was prepared with cases organised according to strain rate. The Anand model was implemented using the previously determined material parameters. The same temperatures and strain rates as in the experiment were applied in the simulations. The geometric model included the sample (⌀10 mm, height 12 mm) and two anvils (25 × 25 × 5 mm – Figure 4), which acted as compressive elements and were modelled as rigid bodies. The sample material was defined using the Anand model. The geometric model was created in SolidWorks 2021 and imported into Ansys Workbench 2020, where a "static structural" analysis with large deformations was applied. The Anand constants were entered in "Engineering Data," along with the temperature-dependent Young's modulus—110 GPa at room temperature [15]—with missing data estimated from experimental plots [33] (Table 5 and Figure 5). The mesh was constructed from hexahedral elements

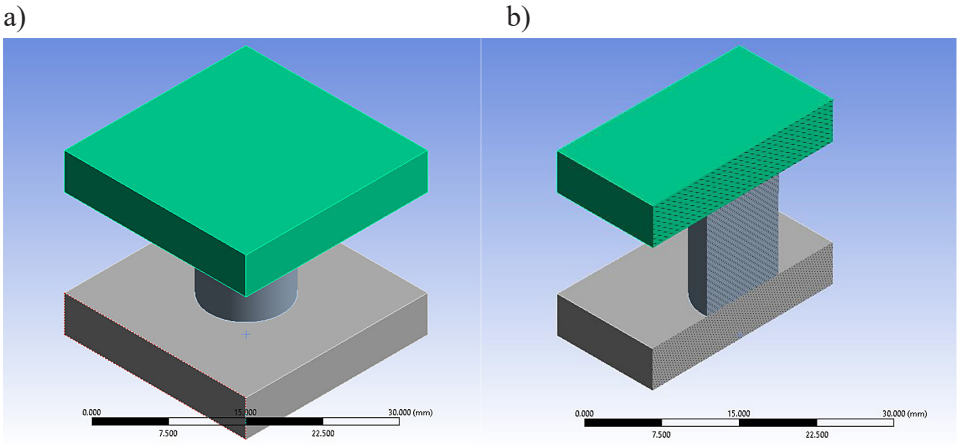

Figure 4. Geometrical model used in analysis. Full view (a) and cross-section view (b)

Table 5. Young's modulus of Grade 2 titanium as a function of temperature

Temperature [C]	Young's modulus [MPa]	Poisson's ratio	Bulk modulus [Pa]	Shear modulus [Pa]
20	1.1e+05	0.37	1.41e+11	4.01e+10
400	8450	0.37	1.08e+10	3.08e+09
500	5580	0.37	7.15e+09	2.04e+09
600	4500	0.37	5.77e+09	1.64e+09

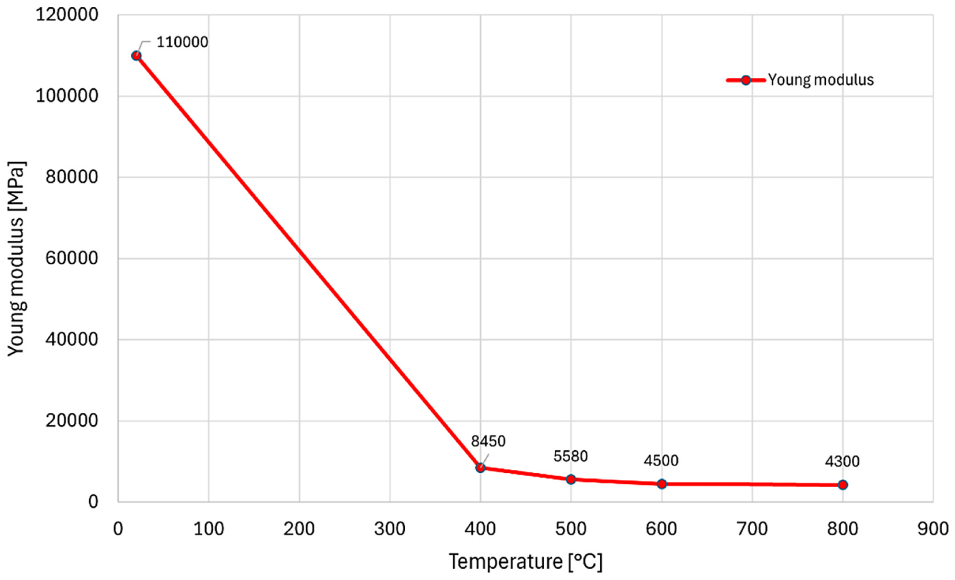

Figure 5. Young's modulus of Grade 2 titanium as a function of temperature

with a size of 1 mm, resulting in 3.874 elements and 18,357 nodes (Figure 6). Tests showed that further mesh refinement did not improve results but only increased computation time. The compression simulation was performed by displacing the upper anvil 7 mm toward the lower one—matching the actual displacement—over a time dependent on the strain rate. Each simulation was divided into 10 steps, and the sample was assigned a uniform temperature corresponding to the given case. In total, 25 cases were solved: 5 strain rates (0.01–10 s^{-1}, including 5 s^{-1}) for 5 temperatures (400–800 °C). The computation time for a single run ranged from 5 to 15 minutes. An iterative PCG (Preconditioned Conjugate Gradient) solver was used, which is effective for nonlinear large-deformation analysis.

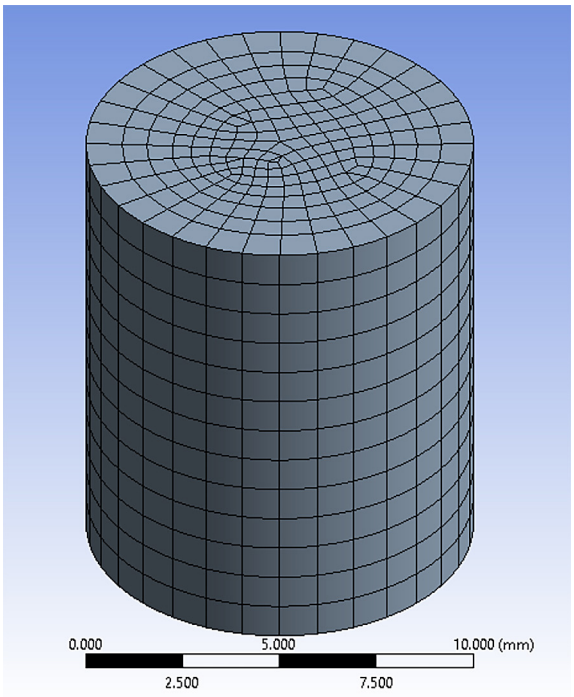

Figure 6. Sample meshed with finite elements

RESULTS

In terms of grain refinement, the best results were obtained for the samples compressed at temperatures of 500–600 °C and strain rates of 0.1–1 s^{-1} [21]. Therefore, the following presentation focuses on these conditions. Curves drawn with a solid line represent experimental results, while those with markers correspond to finite element simulation results (Figures 7 and 10).

The Anand model reproduced the stress response most accurately at strain rates of 0.01 s^{-1} and 0.1 s^{-1}, and in the initial phase for 1 s^{-1} and 10 s^{-1}. For the theoretical strain rate of 5 s^{-1}, the sample behaviour was reproduced correctly by the model (Figure 5). However, the curve lies slightly closer to the 1 s^{-1} strain rate than to 10 s^{-1}, indicating the need for further refinement of the

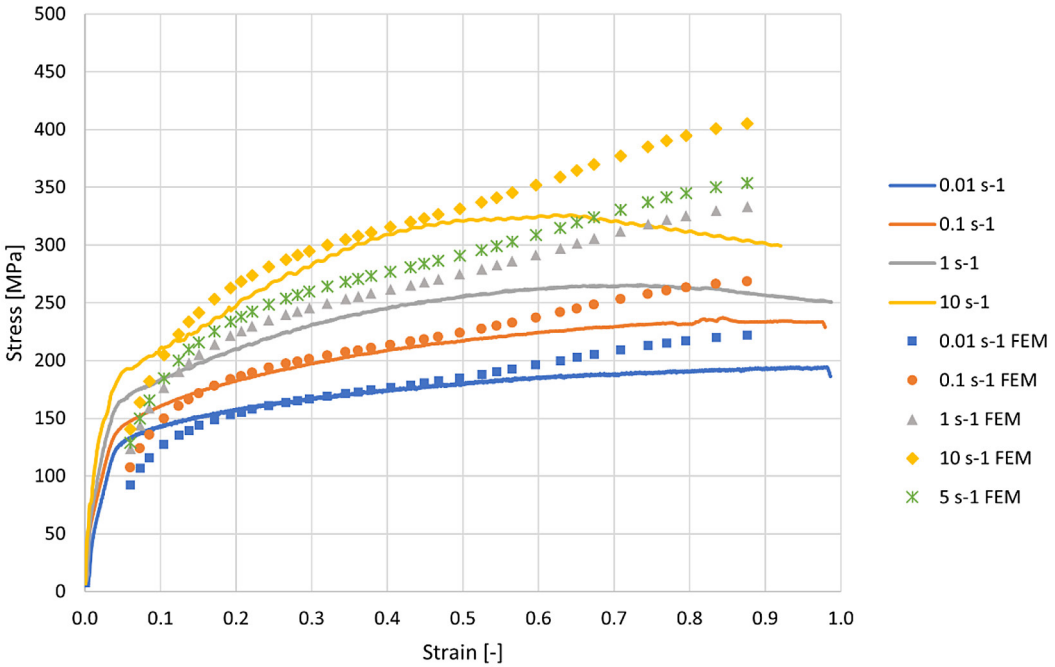

Figure 7. Comparison of FEM simulation results and experimental curves at 500 °C

Anand model parameters. A significant difference is observed – the model deviates from the experimental results in the third stage of TMP. Figure 8 shows the normal axial stress distribution at a temperature of 500 °C and a strain rate of 0.1 s^{-1}. The centre recorded a value of 260 MPa, the side 190 MPa, and the edge 340 MPa. At the final stage of the analysis, these values were approximately 30–40 MPa higher than in the experiment. Stress concentrations are as expected and overall model behaviour is similar to the real life sample.

For the analysis at a strain rate of 1 s^{-1} (Figure 9), the final stresses deviate even more clearly from the experimental results. At higher strain rates, the experimental curves show a drop in stress, which the Anand model does not reproduce. The recorded stresses were 320 MPa at the centre, 240 MPa at the side, and 420 MPa at the edge. The next series

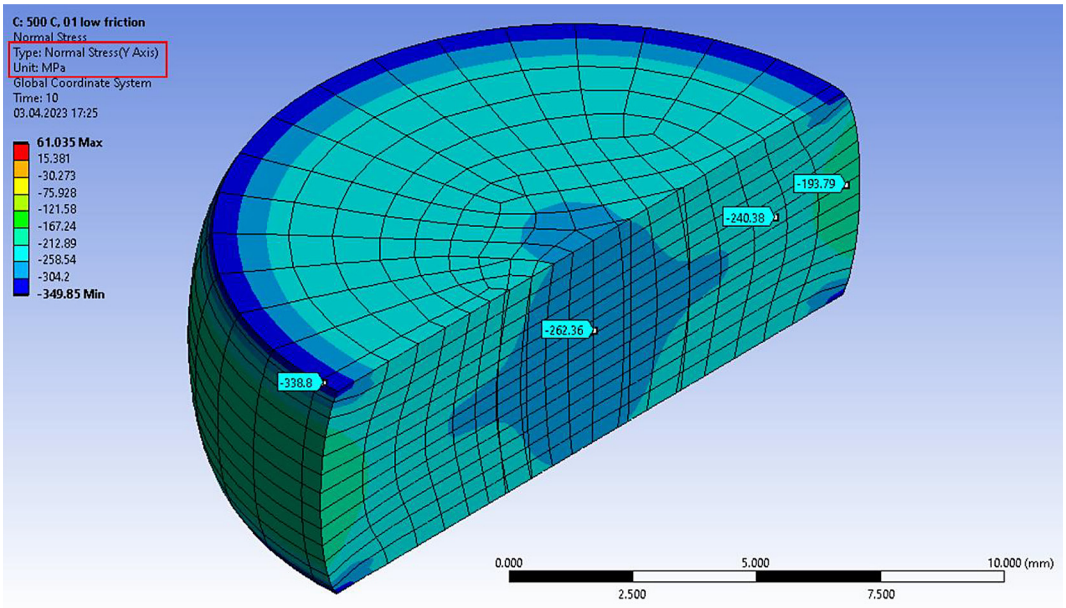

Figure 8. Axial normal stress distribution calculated using FEM for the case of 500 °C and 0.1 s^{-1}. Values visible on cyan probes are in MPa

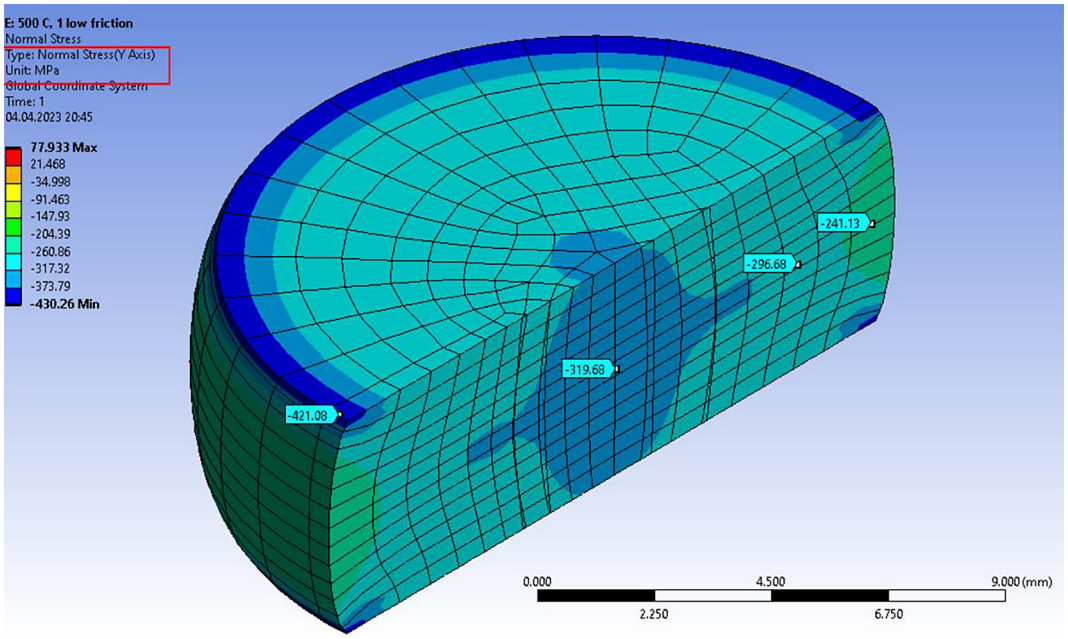

Figure 9. Axial normal stress distribution calculated using FEM for the case of 500 °C and 1 s^{-1}. The values visible on cyan probes are in MPa

of analyses concerns a temperature of 600 °C. As before, good agreement between the model and experimental data is observed in the initial phase of plastic deformation. As deformation progresses, discrepancies gradually increase. In this case, the model predicts the onset of plastic flow at a slightly higher true strain than in the experiment. Similarly, the 5 s^{-1} test aligns more closely with the 1 s^{-1} result than with 10 s^{-1} (Figure 10). The stress distribution is very similar to that observed for the 500 °C case. At a strain rate of 0.1 s^{-1}, the stresses are approximately 190 MPa at the centre, 150 MPa at the side, and 240 MPa at the edge (Figure 11). At a strain rate of 1 s^{-1} (Figure 12), the stresses are 235 MPa at the centre, 173 MPa at the side, and 290 MPa at the most heavily loaded edge locations.

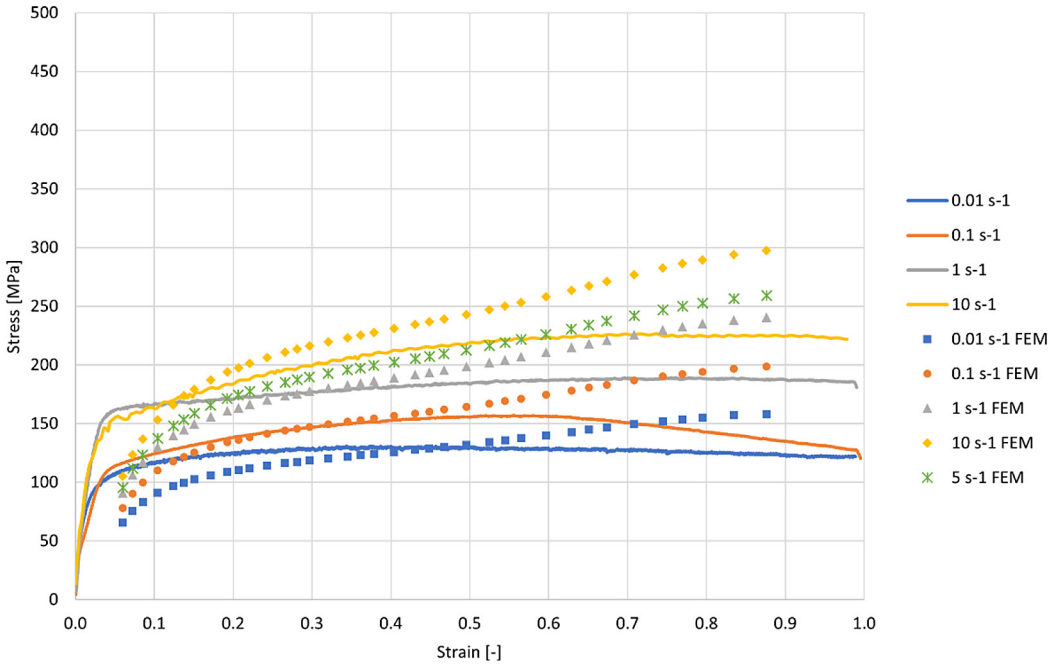

Figure 10. Comparison of FEM simulation results and experimental curves at 600 °C

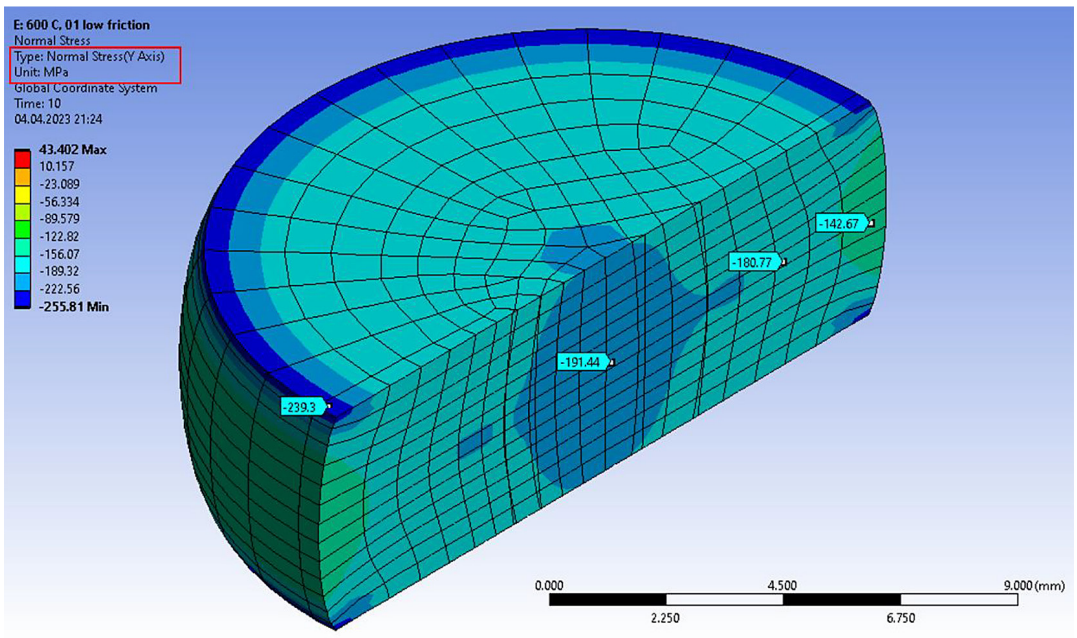

Figure 11. Axial normal stress distribution calculated using FEM for the case of 600 °C and 0.1 s^{-1}. Values visible on cyan probes are in MPa

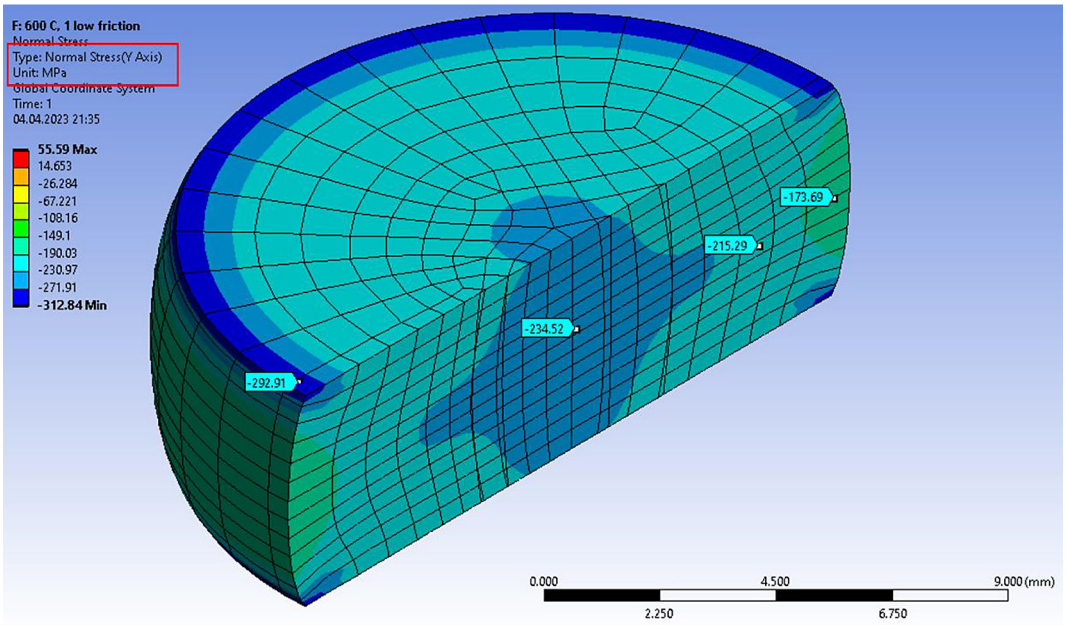

Figure 12. Axial normal stress distribution calculated using FEM for the case of 600 °C and 1 s^{-1}. Values visible on cyan probes are in MPa

DISCUSSION AND CONCLUSIONS

Although the Anand model is unconventional for this type of process, it provided good agreement between simulation results and experiments in the initial phase of deformation (particularly for 500–600 °C and 0.1–1 s^{-1}). An important observation made during the study was its ability to reproduce the stress evolution in the elastic compression phase. However, this behaviour is strongly temperature-dependent—the higher the temperature, the smoother the transition from elastic to plastic deformation.

The several constitutive models were considered but there is several reasons why Anand was chosen. The separable Johnson–Cook law reproduces quasi-steady plastic flow but typically misses the elastic–plastic transition and transient softening in warm/hot deformation of CP-Ti unless ad-hoc modifications are introduced [34, 35]. The Anand model, with an internal state variable for deformation resistance and thermally activated evolution, better captures early-stage response and non-steady rate/temperature histories, while remaining practical for FEM [36]. In the analysed 500–600 °C, 0.1–1 s^{-1} window, Anand provided lower errors and more stable calibration than baseline JC [10]. Strain- and temperature-compensated Arrhenius fits capture peak and steady flow, but are purely phenomenological: many temperature and strain-dependent coefficients, no internal state, and weak performance for transients (rate and temperature changes, elastic–plastic transition). Anand uses an internal resistance variable with thermally activated evolution, so it better handles early-stage response and non-steady paths while maintaining comparable steady-state accuracy in the tested window [10, 11, 20]. KHL improves rate–temperature coupling over JC and can represent mechanisms like twinning, but it involves more parameters and is less readily available in commercial FEM workflows. Anand achieves similar or better fidelity for warm forming with a simpler state variable framework and native FEM support [11, 37].

Comparison of stress–strain curves (Figures 5 and 8) shows that, according to the Anand model, the material enters plastic deformation slightly earlier than in reality. Moreover, the model cannot accurately reproduce the stress drop in the final stage of compression — thermal softening. This is primarily because the model was originally developed for high-temperature viscoplastic deformation of metals where strain hardening and dynamic recovery dominate, but dynamic recrystallisation or flow softening mechanisms are not explicitly included. This limitation arises from the nature of the model itself, which mathematically cannot account for the stress decrease [38, 39]. This stress drop is most likely caused by dynamic recrystallisation leading to secondary grain growth [9, 11, 40]. Augmenting Anand with a DRX internal variable—using

JMAK-type kinetics for the recrystallised fraction and coupling it to the deformation resistance or grain-size-dependent saturation stress—could reproduce the stress drop while preserving the model's good transient behaviour; the trade-off is a modest increase in parameters and the need for microstructural validation [41, 42]. Post-processing and output settings may also influence results. When stress is recorded at every increment, minor oscillations—often inherent to numerical solutions—can appear visually prominent. Such fluctuations usually reflect the discrete nature of numerical integration rather than actual material behaviour. Applying smoothing techniques or averaging over larger strain intervals can help separate numerical noise from meaningful response [43].

The largest observed discrepancy concerns the final shape of the samples. During the experiment (Figure 1), instead of deforming into the expected barrel shape [44, 45], the samples exhibited clear asymmetric deformation, suggesting the occurrence of shear stresses that were not considered in the model. Another possible reason for this behaviour could be a material defect in the rod, which may have been more strengthened in one direction during production. For this reason, prior to experimentation, it is essential to characterise the properties of the material in its initial state, preferably in both longitudinal and transverse directions. If significant anisotropy is identified that could affect the experimental results, the material should be subjected to annealing heat treatment to homogenise its microstructure [46, 47].

The obtained findings—accurate near-saturation flow with baseline Anand and missing post-peak softening at higher rates—align with recent Ti-alloy studies showing that unified or DRX-augmented models outperform separable laws for warm or hot deformation and complex T, $\dot{\varepsilon}$ histories. Zhou et al. [48] coupled flow stress to a DRX kinetics variable for TB8 Ti, which allowed them to reproduce the post-peak softening and microstructure evolution that the analysed baseline Anand (no DRX term) cannot. In contrast, the model adopted in this study achieves low errors in the elastic–plastic transition and near-saturation flow for Grade 2 Ti in 500–600 °C, 0.1–1 s^{-1}, but overestimates late-stage stresses at higher rates—precisely the gap Zhou's DRX coupling is designed to close (at the cost of extra parameters and microstructural calibration). Zhang et al. [49] developed a a unified constitutive model for Ti-55511 in the two-phase region that explicitly couples flow stress to microstructural mechanisms (e.g., DRX, α-spheroidisation), enabling accurate post-peak softening and microstructure predictions across hot-deformation paths. By contrast, this study on Grade 2 Ti used baseline Anand to calibrate a process-oriented window (500–600 °C, 0.1–1 s^{-1}) and matchee the elastic–plastic transition and near-saturation flow, accepting that late-stage softening at higher rates is not captured without DRX coupling. A similar research to that presented in this paper was carried out by Yi et al. [50]. They modelled TC21 using different model (strain compensated Arrhenius law and RBF neural network). The adopted Anand-based approach allowed achieving low errors in the elastic–plastic transition and near-saturation flow while acknowledging the need for DRX coupling to capture post-peak softening.

Despite limitations, the model shows fairly good agreement with reality—the differences in predicted stresses are not significant, and the shape of the curve almost perfectly matches the experimental curve in the first (most critical) phase of TMP. The calibrated Anand-based FEM allows narrowing the TMP window (500–600 °C; 0.1–1 s^{-1}) before physical trials, so experimental work is focused on a few confirmatory runs rather than broad exploration. Overall, the workflow shifts cost from material and machine time to inexpensive computation. This directly supports implant manufacturing by sizing billets and first-pass reductions for preform upsetting/forging (e.g., hip stems, dental screws, trauma plates) and by providing the information on press tonnage, die stiffness, and cycle time. As post-peak softening at higher rates is not captured, targeted validations or an optional DRX-coupled extension are recommended when such passes are required. Incorporating measured anisotropy in future work will further improve process-specific predictions. It can be concluded that the Anand model enables prediction of stress evolution in the cases not experimentally tested and may be useful for planning and optimising TMP processes for commercially pure titanium.

REFERENCES

1. Zhang L. and Chen L., A review on biomedical titanium alloys: recent progress and prospect, Adv Eng Mater, Apr. 2019; 21(4): 1801215.
2. Hussain O., Saleem S., and Ahmad B., Implant

materials for knee and hip joint replacement: A review from the tribological perspective, *IOP Conf. Ser.: Mater. Sci. Eng.*, Oct. 2019; 561(1): 012007.

3. Rack H. J. and Qazi J. I., Titanium alloys for biomedical applications, *Materials Science and Engineering: C*, Sep. 2006; 26(8): 1269–1277.
4. Gomes C. C., Moreira L. M., V. Santos V. J. S., Ramos A. S., Lyon J. P., Soares C. P., and Santos F. V., Assessment of the genetic risks of a metallic alloy used in medical implants, *Genet. Mol. Biol.*, Jan. 2011; 34(1): 116–121.
5. Khadija G., Saleem A., Akhtar Z., Naqvi Z., Gull M., Masood M., Mukhtar S., Batool M., Saleem N., Rasheed T., Nizam N., Ibrahim A., and Iqbal F., Short term exposure to titanium, aluminum and vanadium (Ti 6Al 4V) alloy powder drastically affects behavior and antioxidant metabolites in vital organs of male albino mice, *Toxicology Reports*, 2018; 5: 765–770.
6. Quinn J., McFadden R., Chan C.-W., and Carson L., Titanium for orthopedic applications: an overview of surface modification to improve biocompatibility and prevent bacterial biofilm formation, *iScience*, Nov. 2020; 23(11): 101745.
7. Garbacz H., Wieciński P., Kuczyńska D., Kubacka D., and Kurzydłowski K. J., The effect of grain size on the surface properties of titanium grade 2 after different treatments, *Surface and Coatings Technology*, Feb. 2018; 335: 13–24.
8. Kawałko J., Wroński M., Bieda M., Sztwiertnia K., Wierzbanowski K., Wojtas D., Łagoda M., Ostachowski P., Pachla W., and Kulczyk M., Microstructure of titanium on complex deformation paths: Comparison of ECAP, KOBO and HE techniques, *Materials Characterization*, Jul. 2018; 141: 19–31.
9. Zeng Z., Zhang Y., and Jonsson S., Deformation behaviour of commercially pure titanium during simple hot compression, *Materials & Design*, Sep. 2009; 30(8): 3105–3111.
10. Bańczerowski J. and Pawlikowski M., New approach in constitutive modelling of commercially pure titanium thermo-mechanical processing," *Continuum Mech. Thermodyn.*, Sep. 2021; 33(5): 2109–2121.
11. Lin Y. C. and Chen X.-M., A critical review of experimental results and constitutive descriptions for metals and alloys in hot working, *Materials & Design*, Apr. 2011; 32(4): 1733–1759.
12. Khan A. S., Sung Suh Y., and Kazmi R., Quasi-static and dynamic loading responses and constitutive modeling of titanium alloys, *International Journal of Plasticity*, Dec. 2004; 20 (12): 2233–2248.
13. Brown S., Kim K., and Anand L., An internal variable constitutive model for hot working of metals, *International Journal of Plasticity*, 1989; 5(2): 95–130.
14. Anand L., Constitutive equations for hot-working of metals, *International Journal of Plasticity*, 1985; 1(3): 213–231.
15. Balasubramanian S. and Anand L., Plasticity of initially textured hexagonal polycrystals at high homologous temperatures: application to titanium, *Acta Materialia*, Jan. 2002; 50(1): 133–148.
16. Bańczerowski J. and Pawlikowski M., Numerical and experimental analysis of thermoplastic deformation in pure titanium using the Anand model for biomedical implant design, *Adv. Sci. Technol. Res. J.*, Sep. 2025; 19(9): 504–515.
17. Dziubińska A., Majerski K., and Winiarski G., Investigation of the Effect of Forging Temperature on the Microstructure of Grade 5 Titanium ELI, *Adv. Sci. Technol. Res. J.*, Dec. 2017; 11(4): 147–158.
18. Chandrasekaran M., Forging of metals and alloys for biomedical applications, in *Metals for Biomedical Devices*, Elsevier, 2019; 293–310.
19. Xu M., Xiao Q., Zu X., Tan Y., and Huang Z., Constitutive modeling of annealed OFHC with wide strain-rate and temperature effects: Incorporating dislocation dynamics and normalized microstructural size evolution, *Materials (Basel)*, Sep. 2023; 16(19): 6517.
20. Kareem S. A., Anaele J. U., Aikulola E. O., Olanrewaju O. F., Omiyale B. O., Bodunrin M. O., and Alaneme K. K., Hot deformation behaviour, constitutive model description, and processing map analysis of superalloys: An overview of nascent developments, *Journal of Materials Research and Technology*, Sep. 2023; 26: 8624–8669.
21. Bańczerowski J., Pawlikowski M., Płociński T., Zagórski A., Sawicki S., and Gieleta R., New approach to α-titanium mechanical properties enhancement by means of thermoplastic deformation in mid-temperature range, *Continuum Mech. Thermodyn.*, Nov. 2024; 36(6): 1645–1660.
22. Nemat-Nasser S., Guo W. G., and Cheng J. Y., Mechanical properties and deformation mechanisms of a commercially pure titanium, *Acta Materialia*, Oct. 1999; 47(13): 3705–3720.
23. Parvizi S., Hashemi S. M., Asgarinia F., Nematollahi M., and Elahinia M., Effective parameters on the final properties of NiTi-based alloys manufactured by powder metallurgy methods: A review, *Progress in Materials Science*, Apr. 2021; 117: 100739.
24. Zeng Z., Zhang Y., and Jonsson S., Microstructure and texture evolution of commercial pure titanium deformed at elevated temperatures, *Materials Science and Engineering: A*, Jul. 2009; 513–514: 83–90.
25. Ahn K., Huh H., and Yoon J., Rate-dependent hardening model for pure titanium considering the effect of deformation twinning, *International Journal of Mechanical Sciences*, Jul. 2015; 98: 80–92.
26. Bishoyi B. D., Sabat R. K., Sahu J., and Sahoo S. K., Effect of temperature on microstructure and texture

evolution during uniaxial tension of commercially pure titanium, *Materials Science and Engineering: A*, Aug. 2017; 703: 399–412.

27. Banerjee S. and Mukhopadhyay P., *Phase Transformations: Examples from Titanium and Zirconium Alloys*. Elsevier, 2010.
28. Franklin S. V., Mertens F., and Marder M., Portevin--Le Chatelier effect, *Phys. Rev. E*, Dec. 2000; 62(6): 8195–8206.
29. Prasad K. and Varma V. K., Serrated flow behavior in a near alpha titanium alloy IMI 834, *Materials Science and Engineering: A*, Jul. 2008; 486(1–2): 158–166.
30. Balasubramanian S. and Anand L., Elasto-viscoplastic constitutive equations for polycrystalline fcc materials at low homologous temperatures, *Journal of the Mechanics and Physics of Solids*, Jan. 2002; 50(1): 101–126.
31. Balasubramanian R., Nagumothu R., Parfenov E., and Valiev R., Development of nanostructured titanium implants for biomedical implants – A short review, *Materials Today: Proceedings*, 2021; 46: 1195–1200.
32. Cheng Z. N., Wang G. Z., Chen L., Wilde J., and Becker K., Viscoplastic Anand model for solder alloys and its application, *Soldering & Surface Mount Technology*, Aug. 2000; 12(2): 31–36.
33. Bańczerowski J., Proces technologiczny oraz modelowanie numeryczne obróbki termoplastycznej tytanu na potrzeby inżynierii biomedycznej, Rozprawa doktorska, Politechnika Warszawska, Warszawa, 2023.
34. Liang R. and Khan A. S., A critical review of experimental results and constitutive models for BCC and FCC metals over a wide range of strain rates and temperatures, *International Journal of Plasticity*, Jan. 1999; 15(9): 963–980.
35. Ashrafian M. M. and Hosseini Kordkheili S. A., Plastic temperature-dependent constitutive modeling of pure aluminum diaphragms at large strains by using bulge test, *Journal of Materials Research and Technology*, Mar. 2021; 11: 412–427.
36. Grama S. N., Subramanian S. J., and Pierron F., On the identifiability of Anand visco-plastic model parameters using the Virtual Fields Method, *Acta Materialia*, Mar. 2015; 86: 118–136.
37. Singh A. K., Kumar A., Narasimhan K., and Singh R., Understanding the deformation and fracture mechanisms in backward flow-forming process of Ti-6Al-4V alloy via a shear modified continuous damage model, *Journal of Materials Processing Technology*, Jun. 2021; 292: 117060.
38. Chen X., Chen G., and Sakane M., Prediction of stress-strain relationship with an improved Anand constitutive Model For lead-free solder Sn-3.5Ag, *IEEE Trans. Comp. Packag. Technol.*, Mar. 2005; 28(1): 111–116.
39. Zhang Z., Chen Z., Liu S., Dong F., Liang K., and Ma K., The comparison of Qian-Liu model and Anand model for uniaxial tensile test of SAC305, in *2019 20th International Conference on Electronic Packaging Technology(ICEPT)*, Hong Kong, China, 2019; 1–5.
40. Zhang L., Pellegrino A., Townsend D., and Petrinic N., Thermomechanical constitutive behaviour of a near α titanium alloy over a wide range of strain rates: Experiments and modelling, *International Journal of Mechanical Sciences*, Jan. 2021; 189: 105970.
41. Shu A., Zhou J., Ren J., and Wang Z., A modified constitutive model considering dynamic recrystallization behavior for cutting Inconel 718, *Journal of Manufacturing Processes*, Oct. 2023; 104: 189–204.
42. Liu G., Mao C., Ding R., Yu L., Liu C., and Liu Y., The kinetics of dynamic recrystallization and construction of constitutive modeling of RAFM steel in the hot deformation process, *Journal of Nuclear Materials*, Dec. 2021; 557: 153285.
43. Franz S., Post-processing and improved error estimates of numerical methods for evolutionary systems, *IMA Journal of Numerical Analysis*, Sep. 2024; 44(5): 2936–2958.
44. Ye X., Gong X., Yang B., Li Y., and Nie Y., Deformation inhomogeneity due to sample–anvil friction in cylindrical compression test, *Transactions of Nonferrous Metals Society of China*, Feb. 2019; 29(2): 279–286.
45. Dhir R. K. and Sangha C. M., Relationships between size, deformation and strength for cylindrical specimens loaded in uniaxial compression, *International Journal of Rock Mechanics and Mining Sciences & Geomechanics Abstracts*, Nov. 1973; 10(6): 699–712.
46. Sheyko S., Belokon Y., Hrechanyi O., and Vasilchenko T., *Thermoplastic Processing of Structural Metallic Materials: Experiments, Theory, and Modeling*. Springer Nature, 2024.
47. Moreno-Valle E. C., Pachla W., Kulczyk M., Savoini B., Monge M. A., Ballesteros C., and Sabirov I., Anisotropy of uni-axial and bi-axial deformation behavior of pure Titanium after hydrostatic extrusion, *Materials Science and Engineering: A*, Dec. 2013; 588: 7–13.
48. Zhou C., Cao F., Yang Z., and Rao W., Dynamic Recrystallization Constitutive Model and Texture Evolution of Metastable β Titanium Alloy TB8 during Thermal Deformation, *Materials (Basel)*,, Mar. 2024; 17(7): 1572.
49. Zhang H., Lin Y. C., Su G., Xie Y., Qiu W., Zeng N., Zhang S., and Wu G., Hot deformation physical mechanisms and a unified constitutive model of a solid solution Ti55511 alloy deformed in the two-phase region, *Journal of Materials Research and Technology*, Jan. 2025; 34: 1591–1610.
50. Yi S.-X., Yang Z.-J., and Xie H.-X., Hot deformation and constitutive modeling of TC21 titanium alloy, *Materials*, Jan. 2022;15(5): 1923.